

# Design and Evolution of a Triad Twisted String Actuator for Controlling a Two Degrees of Freedom Joint: Improving Performance and Investigating Active Transmission Adjustment

Damian Crosby<sup>1</sup>, Joaquin Carrasco<sup>2</sup>, William Heath<sup>2</sup>, Lutong Li<sup>1</sup>, and Andrew Weightman<sup>1</sup>

Journal Title  
XX(X):1–13  
©The Author(s) 0000  
Reprints and permission:  
[sagepub.co.uk/journalsPermissions.nav](http://sagepub.co.uk/journalsPermissions.nav)  
DOI: 10.1177/ToBeAssigned  
[www.sagepub.com/](http://www.sagepub.com/)



## Abstract

Actuated universal joints are used in a wide range of robotic applications, including mobile snake robots, snake-arm robots and robotic tails. Depending on the application and design constraints, these can use remote cable or fluid driven systems, or inline motors. In order to realise the benefits of inline actuation while keeping the system compact with a high power to weight ratio, an actuated universal joint (AUJ) was developed using an “antagonistic triad” of three twisted string actuators in our previous work. However, the design of this system had numerous drawbacks in its prototype form, namely a limited angle range, poor accuracy due to the angular feedback sensors used, and issues with string failure due to mechanical design choices. In this publication, we identify and address these challenges through design changes, and as a result angle range was increased from  $\pm 14.50^\circ$  to  $\pm 26.00^\circ$  for a single axis, and  $\pm 6.00^\circ$  to  $\pm 20.00^\circ$  for a dual axis movement.

## Keywords

Flexible Robots, Force Control, Tendon/Wire Mechanism

## 1 Introduction

Actuated universal joint (AUJ) mechanisms are crucial in various robotic applications like confined space inspection with continuum robots, highly manoeuvrable snake robots, and biomimetic robot tails for stability. These mechanisms can either use inline actuators, which directly move the joint (Rezaei et al. 2008; Baba et al. 2010; Wright et al. 2012), or cable/fluid driven systems relying on a static “base” to house actuators or compressors (Qin et al. 2023). Inline actuators necessitate high torque due to lifting the mass of subsequent sections, while systems with a static base require additional space, limiting their utility in mobile robots.

First developed by Würtz et al. (2010), the twisted string actuator (TSA) uses two or more strings between two fixtures as a linear actuator. Rotating one fixture, typically with an electric motor, twists the strings into a helix, decreasing the distance between them, as shown in figure 1. Given the unwound length  $l_u$  in meters, and the cross-section radius of the string  $r_s$  (or  $r_s + r_c$  when there are more than two strings, where  $r_c$  is the radius of a tangentially constrained circle drawn between the strings) in meters as shown in figure 2. The actuator length in meters is given by

$$l_s(\theta_s) = \sqrt{l_u^2 - \theta_s^2 r_s^2}, \quad (1)$$

where  $\theta_s$  is the motor angle in radians. TSA actuators have applications in hand orthoses, elbow joints,

foldable robot arms, and more (Muehlbauer et al. 2021; Park et al. 2020; Suthar and Jung 2021).

Alternative electric actuation systems, like lead-screws, require additional gearing for significant reduction increases, which results in larger and heavier actuators. In contrast, a TSA can achieve reduction increases by reducing string thickness or count, thus slightly reducing actuator mass (Palli et al. 2012). While leadscrews can marginally increase reduction by decreasing thread lead (Budynas and Nisbett 2011), this approach faces challenges related to manufacturing tolerances and material limitations. Increasing screw radius also enlarges actuator size and mass similarly. Therefore, from a mechanical perspective, TSA holds an advantage over leadscrews by increasing reduction without adding mass.

One of TSAs main challenges is its reduction variation with motor angle, exhibiting an inverse nonlinear relationship (Würtz et al. 2010; Palli et al. 2012). String

<sup>1</sup>Department of Mechanical, Aerospace and Civil Engineering, The University of Manchester, UK

<sup>2</sup>Department of Electrical and Electronic Engineering, The University of Manchester, UK

### Corresponding author:

Damian Crosby, School of Engineering, Department of Mechanical, Aerospace and Civil Engineering, Faculty of Science and Engineering, The University of Manchester, M13 9PL, UK

Email: [damian.crosby@manchester.ac.uk](mailto:damian.crosby@manchester.ac.uk)

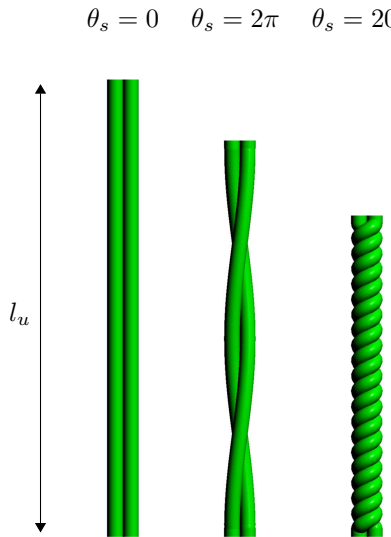


**Figure 1.** The value of  $\theta_s$  increases the number of twists in a string bundle with a string length  $l_u$ .

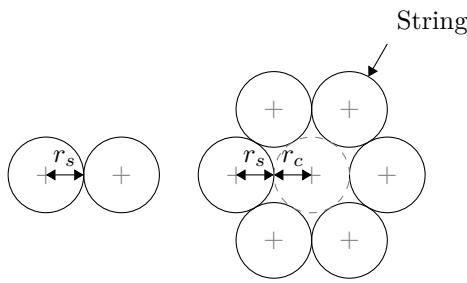


**Figure 2.** The location of  $r_s$  and optionally  $r_c$  in a string bundle.

compliance under high force conditions also requires consideration, which can be addressed through accurate modeling (Nedelchev et al. 2020) or a robust control strategy that disregards compliance in the system model (Würz et al. 2010; Palli et al. 2012). Since TSA can only apply force in tension due to string flexibility, single DOF TSA actuator joints need a spring return mechanism, limiting actuator range as spring force increases with decreasing maximum TSA force (Usman et al. 2017). A linear force return mechanism was developed to partially mitigate this issue, but the ideal solution involves using a second synchronized TSA actuator to achieve a matching antagonistic force profile (Popov et al. 2013; Park et al. 2016; Lee et al. 2019; Park et al. 2020). Thus, a 2 DOF actuator can be realized without springs by adding a third TSA.

The use of TSAs as an actuator for AUJs remains an understudied area of research. Konda et al. (2023) proposed a similar design using a flexible core with continuous curvature instead of a rigid universal joint, presenting an open-loop control solution for multi-axis control using only two TSAs at a time, albeit with a limited azimuthal axis range. In contrast, we demonstrate robust closed-loop control of an AUJ in both axes of motion, covering the full azimuthal range of  $[0, 360]^\circ$ , using three TSAs in an “antagonistic triad” configuration. This results in a light, compact AUJ

design with potential improvements over existing inline actuation options.

Our aim in this publication is to address the issues present in the original design, and analyse and evaluate the performance characteristics and special properties of the TSA antagonistic triad mechanism, in order to prepare it for implementation in a future practical application. As such, we extended our work in (Crosby et al. 2022) by indentifying shortcomings in the original prototype (hereafter referred to as such) and addressing them through design changes to create an “improved prototype” (hereafter referred to as such). We also conducted additional experiments to further characterise the mechanism, by examining the effect of additional follower mass and increased joint velocity. Finally, we have looked at existing snake robots in literature, and have compared how a theoretical robot with this mechanism would compare in terms of performance, specifically the self-supporting segment limit. The main contributions of this work are as follows:

- Identification of improvements that could be made to the original prototype through design changes, and experimental results detailing the performance improvements realised as a consequence.
- Additional experiments conducted to further characterise the performance of the AUJ by the addition of additional mass to the follower and increasing joint velocity.
- A simulation of active transmission adjustment (ATA) which allows the mechanism to change specific performance characteristics in real time during operation.
- Analysis of a theoretical multi-segment antagonistic triad TSA design against existing snake robots.

In section 2 we give a brief summary of the design of the original prototype, in order to furnish the reader with enough information to understand the rest of the publication. More information can be found in (Crosby et al. 2022). In section 3 we identify each improvement we address through design alterations, explain the alterations made, and show the results that demonstrate the improved performance. In section 4 we show the results of additional experiments to further characterise the mechanism. In section 5 we discuss the remaining limitations of the improved prototype, the ATA siumlation, and a distributed control proposal for multi-segment operation. We also compare a theoretical multi-segment design to other snake robots in this section. Finally, section 6 then summarises the publication and discusses future work.

## 2 Original Prototype Design Summary

Because TSA can only operate in tension, a minimum of three TSA are required to operate an AUJ. These can be arranged into an “Antagontic Triad” where adjusting the length of each TSA changes the orientation of the AUJ, in a similar fashion to other

cable driven robotic systems (Qin et al. 2023). These lengths can be combined into a vector function

$$\begin{aligned}\lambda_1(\boldsymbol{\theta}) &= \sqrt{a + 2l_1r \sin(\theta_2) \cos(\theta_1) + l_2^2} \\ \lambda_2(\boldsymbol{\theta}) &= \sqrt{a + b + c - d} \\ \lambda_3(\boldsymbol{\theta}) &= \sqrt{a - b - c + d}\end{aligned}$$

where:

$$\begin{aligned}a &= l_1^2 + 2l_1l_2 \cos(\theta_1) \cos(\theta_2) \\ b &= \sqrt{3}l_1r \sin(\theta_1) - l_1r \sin(\theta_2) \cos(\theta_1) + l_2^2 \\ c &= \sqrt{3}l_2r \sin(\theta_1) \cos(\theta_2) - l_2r \sin(\theta_2) \\ d &= \frac{\sqrt{3}r^2 \sin(\theta_1) \sin(\theta_2)}{2} - \frac{3r^2 \cos(\theta_1)}{2} - \frac{r^2 \cos(\theta_2)}{2} + 2r^2,\end{aligned}\quad (2)$$

where  $\Lambda(\boldsymbol{\theta}) = [\lambda_1(\boldsymbol{\theta}) \ \lambda_2(\boldsymbol{\theta}) \ \lambda_3(\boldsymbol{\theta})]$  is a vector function which outputs the magnitudes of each point pair, and therefore the lengths of each actuator, assuming both ends of each actuator can rotate freely on both  $x$  and  $y$  axes. Other coefficients are labelled in figure 3.

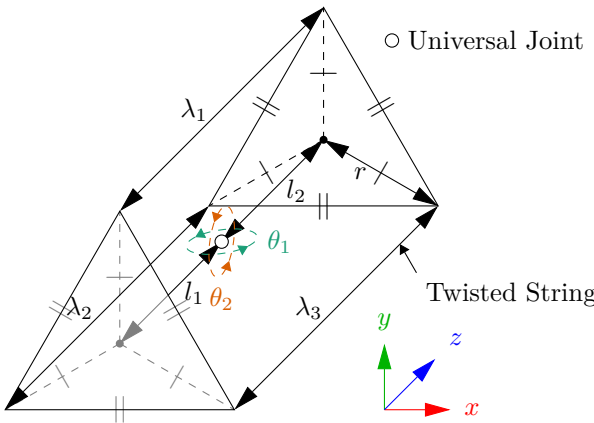


**Figure 3.** Kinematic diagram of the antagonistic triad, where the universal joint rotation is defined by  $\theta_{1,2}$  on the  $y$  and  $x$  axes respectively, and the actuator lengths are defined by  $\lambda_{1,2,3}$  for the *top*, *left* and *right* strings, and  $r$  and  $l_{1,2}$  define the anchor points of the strings.

After an investigation into a position based kinematic control system in the original prototype proved unsuccessful, a force based control system was developed, which uses the inverse dynamics of the AUJ to convert angular velocity from a PID controller into angular torque, which is then turned into force setpoints for each TSA using an optimising algorithm based on (Dessen 1986). The control system is a four layer cascade design, joining an outer loop PID controller  $C_1$  to an inverse dynamic control system  $C_2$  (Spong et al. 2020), to the triad force controller  $C_3$  in (Dessen 1986), to a proportional controller  $C_4$  for each TSA. It uses feedback signals of the joint position and TSA force.

$C_3$  uses the *inverse force transformation* algorithm from (Dessen 1986) with the jacobian of (2) to select an optimal force vector from the desired joint torque. Here it is presented in an unexpanded and more general form,

$$\begin{aligned}J_\Lambda &= \begin{bmatrix} \frac{\partial \lambda_1}{\partial \theta_1} & \frac{\partial \lambda_2}{\partial \theta_1} & \frac{\partial \lambda_3}{\partial \theta_1} \\ \frac{\partial \lambda_1}{\partial \theta_2} & \frac{\partial \lambda_2}{\partial \theta_2} & \frac{\partial \lambda_3}{\partial \theta_2} \end{bmatrix} \\ \gamma(i) &= -J_{\Lambda_{-i,*}}^{-\top} \left( J_{\Lambda_{i,*}}^\top f_{\min} + \tau \right) \\ F(\tau, \boldsymbol{\theta}) &= \begin{bmatrix} f_{\min} & \gamma(2)_1 & \gamma(3)_1 \\ \gamma(1)_1 & f_{\min} & \gamma(3)_2 \\ \gamma(1)_2 & \gamma(2)_2 & f_{\min} \end{bmatrix}.\end{aligned}\quad (3)$$

A force matrix  $F$  is created from the torque input  $\tau$ , jacobian  $J_\Lambda$  from the vector function  $\Lambda$  as defined in equation 2, and minimum force constant  $f_{\min}$ .  $f_{ii}$  is equal to  $f_{\min}$ , while the other elements in the column are based on a calculation using  $J_{\Lambda_{-i,*}}$  where  $-i$  is a row removed from the matrix. Algorithm 1 is then used to create output force vector  $\mathbf{f}$ , which minimises the net force on all TSA while producing the desired output torque on the universal joint.

**Algorithm 1** Selects one column of  $F$  to be the output force vector  $\mathbf{f}$ , where  $\top$  and  $\perp$  are boolean *true* and *false* respectively, and  $f_{*,i}$  is the  $i$ th column of  $F$ .

---

```

1:  $s \leftarrow [\top \ \top \ \top]$ 
2: if  $f_{23} > f_{\min}$  then  $s_2 \leftarrow \perp$  else  $s_3 \leftarrow \perp$  end if
3: if  $f_{31} > f_{\min}$  then  $s_3 \leftarrow \perp$  else  $s_1 \leftarrow \perp$  end if
4: if  $f_{12} \geq f_{\min}$  then  $s_1 \leftarrow \perp$  else  $s_2 \leftarrow \perp$  end if
5: for  $i = 1$  to  $3$  do
6:   if  $s_i \rightarrow \top$  then  $f_{\text{set}} \leftarrow f_{*,i}$  end if
7: end for

```

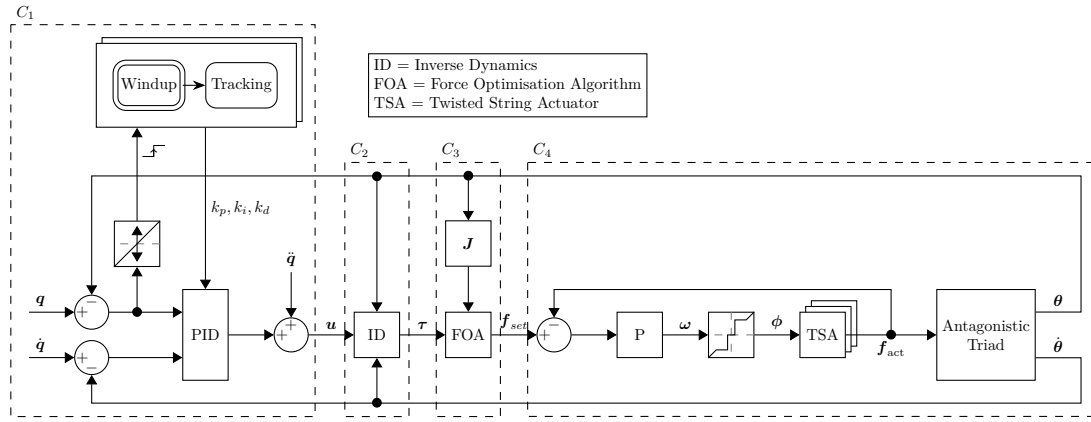
---

Figure 4 shows a complete block diagram of the control system.

## 2.1 Original Prototype Limitations

After the experiments were conducted on the original prototype in (Crosby et al. 2022), several shortcomings with the design were noted that reduced the performance of the system:

- **Limited AUJ Angle Range** - The AUJ angle tracking experiments in (Crosby et al. 2022) only had a range of  $\pm 14.50^\circ$  in a single axis, and  $\pm 6.00^\circ$  for both axes. This was because one or more TSA would completely “unwind” near that limit and be unable to lengthen further. This limits the practicality of such a mechanism, for example a multi-segment design would have a very large minimum curvature. Increasing  $f_{\min}$  does increase the angle range marginally by increasing the TSA motor angle at  $\boldsymbol{\theta} = [0 \ 0]^\top$ , which was proven experimentally, as shown by experiments conducted on the original prototype in figure 5. These experiments were able to achieve modest increases of  $4.00^\circ N^{-1}$  for the positive (upper) limit of the universal joint roll  $\theta_1$ , and  $-6.06^\circ N^{-1}$  for the negative (lower) limit, within the  $f_{\min}$  interval [3, 3.5]. However, further attempts to increase  $f_{\min}$ , or attempts to perform the same experiment on the pitch axis resulted in premature string failure. It was also clear to



**Figure 4.** Block diagram of the complete experimental control system, excluding the hardware velocity controllers for the motors. Dashed boxes correspond to the control layers  $C_1 \dots 4$ .

achieve significant increases in AUJ angle range, a different approach would be needed that would require modifications to the design.

- **Poor AUJ Angle Measurement Accuracy -**

The original prototype used a Bosch Sensortec BNO080 9 degree of freedom (DOF) inertial measurement unit (IMU) (BNO080 Data Sheet) to measure the AUJ orientation. The original plan was to use two IMUs, on the base and follower bodies, and the orientation would be calculated from the difference. However, the magnetometer measurements proved to be unreliable inside the laboratory, so only a single IMU was used and the base segment was orientated with the gravity vector parallel to the  $z$  axis. due to inconsistent magnetometer readings inside the laboratory, only one IMU was implemented, aligning the base body with gravity along the  $z$  axis. This allowed the AUJ orientation to be calculated from only the accelerometer readings, but meant the mechanism could only be controlled when orientated in the vertical axis. There was also an issue with the IMU resolution, which was only accurate to within  $\pm 1.50^\circ$  (BNO080 Data Sheet). A Savitsky-Golay filter was applied to the results in (Crosby et al. 2022) for data presentation purposes and to more accurately represent the true AUJ angles at that point in time.

Also, to enable the mechanism to be controlled in any direction relative to gravity, a solution that can directly measure the mechanical angular displacement of the universal joint was required.

- **String Failures -** One reoccurring issue was

the TSA strings breaking at high values of  $\theta_s$ , which became more common after a number of twisting and untwisting cycles. Occasionally this was caused by a failure of limit monitoring within the control system ( $f > 9$ ), but failure would also occur within normal operating conditions ( $f \leq 9$ ).

### 3 Methodology

#### 3.1 Original Prototype Improvements

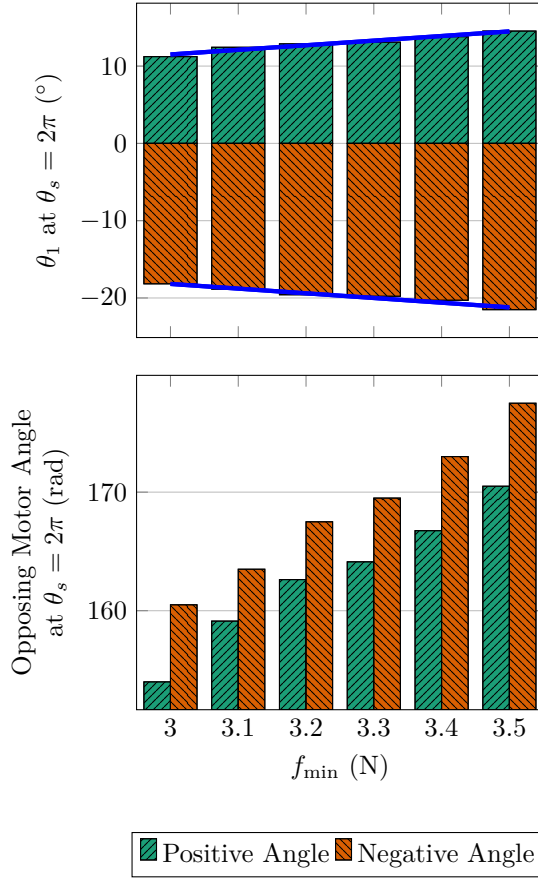


**Figure 5.** AUJ roll angle ( $\theta_1$ ) of the original prototype when the smallest TSA motor angle is equal to  $2\pi$ , and motor angle of the “opposing” TSA (the TSA with the largest motor angle) at the same position.

**3.1.1 Increasing AUJ Angle Range** The most effective modification to improve AUJ angle range is to reduce the value of  $r$  in (2). This decreases the stroke length required for each TSA to achieve the same AUJ angle range as shown by table 1, which also reduces the TSA motor angle accordingly, allowing a greater AUJ angle to be reached before one or more TSA unwind. This can be done by using smaller motors, or by using the same size or larger motors with offset shafts connected by spur gears. Smaller motors were chosen, with a cross section

**Table 1.** Table of the minimum and maximum values of  $\Lambda(\theta)$  at different values of  $r$  in the interval of  $[-\frac{\pi}{2}, \frac{\pi}{2}]$ .

$r$ [mm]	$\lambda_1(\theta)$ [mm]		$\lambda_2(\theta)$ [mm]		$\lambda_3(\theta)$ [mm]	
	Min.	Max.	Min.	Max.	Min.	Max.
13.0	42.64	68.35	42.64	68.57	42.64	68.57
10.0	45.02	64.88	45.02	64.98	45.02	64.98
7.25	47.33	61.78	47.33	61.82	47.33	61.82

of only 120.00 mm<sup>2</sup> compared to 227.00 mm<sup>2</sup> on the existing design. These were Guangdong Kingly Gear Co. Micro Metal Gearmotors (50:1) (JL-12FN20-50-06420), were lighter than the existing motors, 18.00 g compared to 27.00 g, and the mechanism would be less complex. These motors have a much lower  $\theta_{\max}$  than the existing motors of only 44.00 rad s<sup>-1</sup> compared to 442.00 rad s<sup>-1</sup> (DC Micromotors - Precious Metal Commutation), but since the original experiments limited the motor velocity to 10.00 rad s<sup>-1</sup> to ensure mechanism stability, this is not a concern. This change of motors allowed  $r$  to be reduced from 13.00 mm to 7.25 mm.

To achieve this reduction, additional design changes were necessary. The close proximity of the TSA strings made a central shaft impractical, unlike in the original prototype. Instead, a “hollow spider” arrangement was adopted for the universal joint, allowing the TSA strings to pass through its center, as shown in Figure 6. This modification also provided space for directly installing AUJ angle sensors onto the universal joint, as detailed in Section 3.1.2.

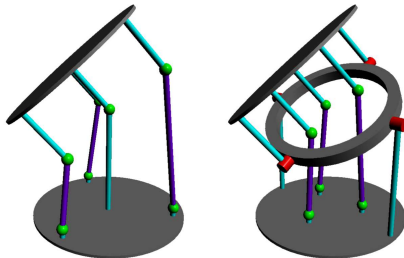


**Figure 6.** An AUJ with a central universal joint, and one with a hollow spider. The hollow spider allows  $r$  to be decreased as space is no longer required for a central universal joint.

**3.1.2 Improving AUJ Angle Measurement Accuracy**  
 Two options were considered to address this issue: potentiometers and hall effect sensors. A potentiometer would link each universal joint spider axis to a resistive track, altering its resistance based on AUJ orientation and providing an analog voltage signal to the controller. Mechanical stops would ensure the required AUJ angle range could be measured during assembly. Alternatively, a hall effect sensor would use a radially bipolar magnet on the shaft’s end with a hall effect sensor beneath it, providing analog voltage signal or digital data for the axial orientation of the magnet and, consequently, the shaft (Bienczyk 2009). The potentiometer solution, chosen for its simplicity of control integration and integrated mechanical stops, would be simpler to integrate into the existing control

system, requiring only an analog to digital converter (ADC) and a slope-intercept form for conversion to an AUJ angle. The Bourns PDB08, selected for its small size and internally threaded shaft, was chosen as the potentiometer (PDB08 - 8 mm Micro Rotary Potentiometer). Operating as a voltage divider at +5.00 V, the PDB08 would offer a resolution of approximately 40.00 ° V<sup>-1</sup>. With the 12-bit resolution of the onboard ADC for myRIO analog inputs, this yields a theoretical resolution of approximately 0.05° compared to ±1.50° for the BNO080. The potentiometer’s sliding noise (maximum 100.00 mV) would reduce this during AUJ motion, partially mitigated with filtering. This improvement from the IMU was deemed significant enough for use in the latest prototype, validated through experimental testing, rendering further investigation of the hall effect sensor unnecessary.

**3.1.3 Preventing String Failure** Analysis of the design revealed “pinch points” and “bite points”, where the string could deform or weaken due to contact with surfaces or sharp edges, as depicted in figure 7a. Removing these points by rounding off edges and using alternative string securing methods, such as tying it into a loop instead of using grub screws, eliminated potential sources of string damage, as shown in figure 7b. However, nylon monofilament, like the TSA string, is still prone to torsion fatigue, reducing its tensile strength. To address this, the SeaKnight BLADE 0.20 mm nylon monofilament was replaced with 0.20 mm Dyneema® polyfilament string, as used in (Palli et al. 2012). Design changes to the string clamp facilitated easier installation of the polyfilament string, making it a practical option.

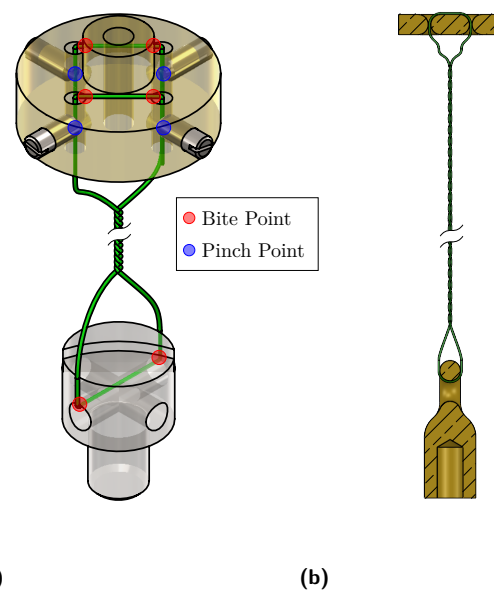


**Figure 7.** (a) The original TSA string loop between the string clamp and capstan bolt, with “pinch” and “bite” points indicated, where premature string failure may occur. (b) Section view of the new TSA string loop showing how the pinch and bite points have been eliminated.

**Table 2.** Model coefficients for the latest prototype.

Coeff.	Value	Coeff.	Value
$l_1$	55.00 mm	$f_{min}$	3.00 N
$l_2$	0.00 mm	$r_s$	200.00 $\mu\text{m}$
$r$	7.25 mm	$m$	61.60 g
$l_u$	55.00 mm	$\dot{\theta}_{s,\max}$	44.00 $\text{rad s}^{-1}$
$\tau_{\max}$	0.04 N m	$\rho$	[0.00 0.00 3.05] mm

Coeff.	Value
$I$	$\begin{bmatrix} 2.80 \times 10^{-5} & 0.00 & 0.00 \\ 0.00 & 2.60 \times 10^{-5} & 0.00 \\ 0.00 & 0.00 & 5.00 \times 10^{-6} \end{bmatrix} \text{kg m}^{-2}$

**Table 3.** PID gains used for the experiment.

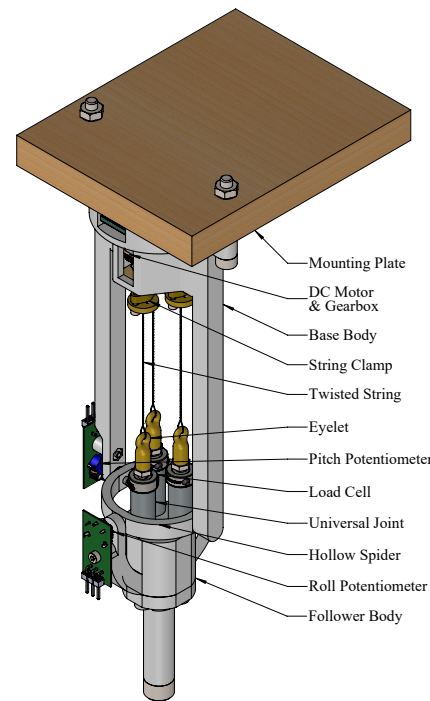
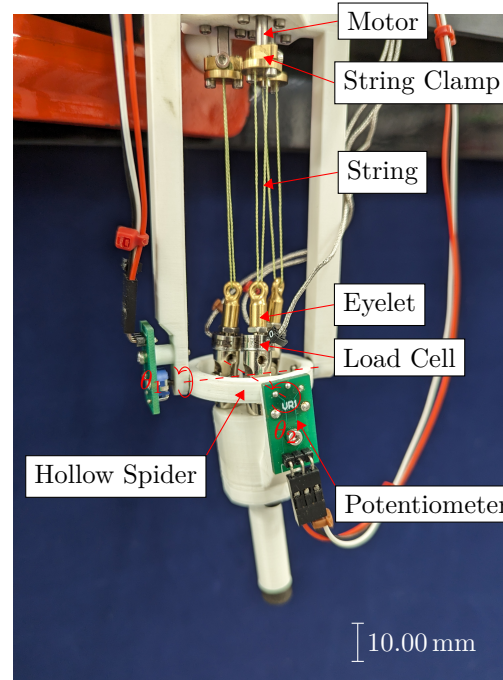
Gain	Value	
	Windup	Tracking
$k_p$	$2.00 \times 10^5$	$8.00 \times 10^5$
$k_i$	3500.00	3500.00
$k_d$	0.00	50.00
$k_{ps}$	5.00	5.00

**3.1.4 Final Design of Improved Prototype** Figure 8 presents an annotated schematic of the improved prototype, and figure 9 shows a photograph with the AUJ axes annotated. The load cells remained unchanged from the original prototype, while alterations were made to the universal joints below them. The hollow spider was connected to the base and follower bodies using machine precision bearings and bushings to ensure smooth motion. Regarding the control system, the Faulhaber MCDC3002 motor controllers (Motion Controllers - Series MCDC 3002 S) were replaced with a single Pimoroni Motor 2040, capable of handling up to four Micro Metal Gearmotors with Micro Metal Motor Encoders attached. Programming was done with a velocity controller similar to the one provided in the *pimoroni-pico* library. Furthermore, the deadband compensation threshold was reduced to  $\pm 0.50 \text{ rad s}^{-1}$  due to the smaller deadband region of the motors, while the motor velocity limit of  $10.00 \text{ rad s}^{-1}$  remained unchanged.

### 3.2 Experimental Comparison of Improved Prototype to Original Prototype

In order to validate and quantify the efficacy of the improvements we made, we conducted two experiments, one to measure the increase in AUJ angle range and another to measure the AUJ angle measurement accuracy. We also did not observe any string failure during normal operation ( $f \leq 9$ ), which demonstrated the efficacy of the improvements made to address that issue. Table 4 shows a summary of the effects of our improvements to the mechanism.

**3.2.1 AUJ Angle Range** To evaluate the expanded AUJ angle range, we replicated the setpoint tracking experiments from (Crosby et al. 2022). Figure 10 illustrates the tracking response in both the pitch and roll axes. Mechanical limitations restricted the AUJ angle range to  $\pm 26.00^\circ$ . This constraint resulted from

**Figure 8.** Schematic of the latest prototype with labelled components.**Figure 9.** Annotated photograph of the single segment physical prototype antagonistic triad, with the roll  $\theta_1$  and pitch  $\theta_2$  axes marked.

the hollow spider colliding with the TSA universal joints in the pitch axis and with the follower body in the roll axis. For the dual-axis trajectory, the angle range was further constrained to  $\pm 20.00^\circ$  due to a load cell exceeding a safety limit of 9.00 N (with the load cell full scale being 9.80 N (LCM100 Miniature In Line Load Cell)).

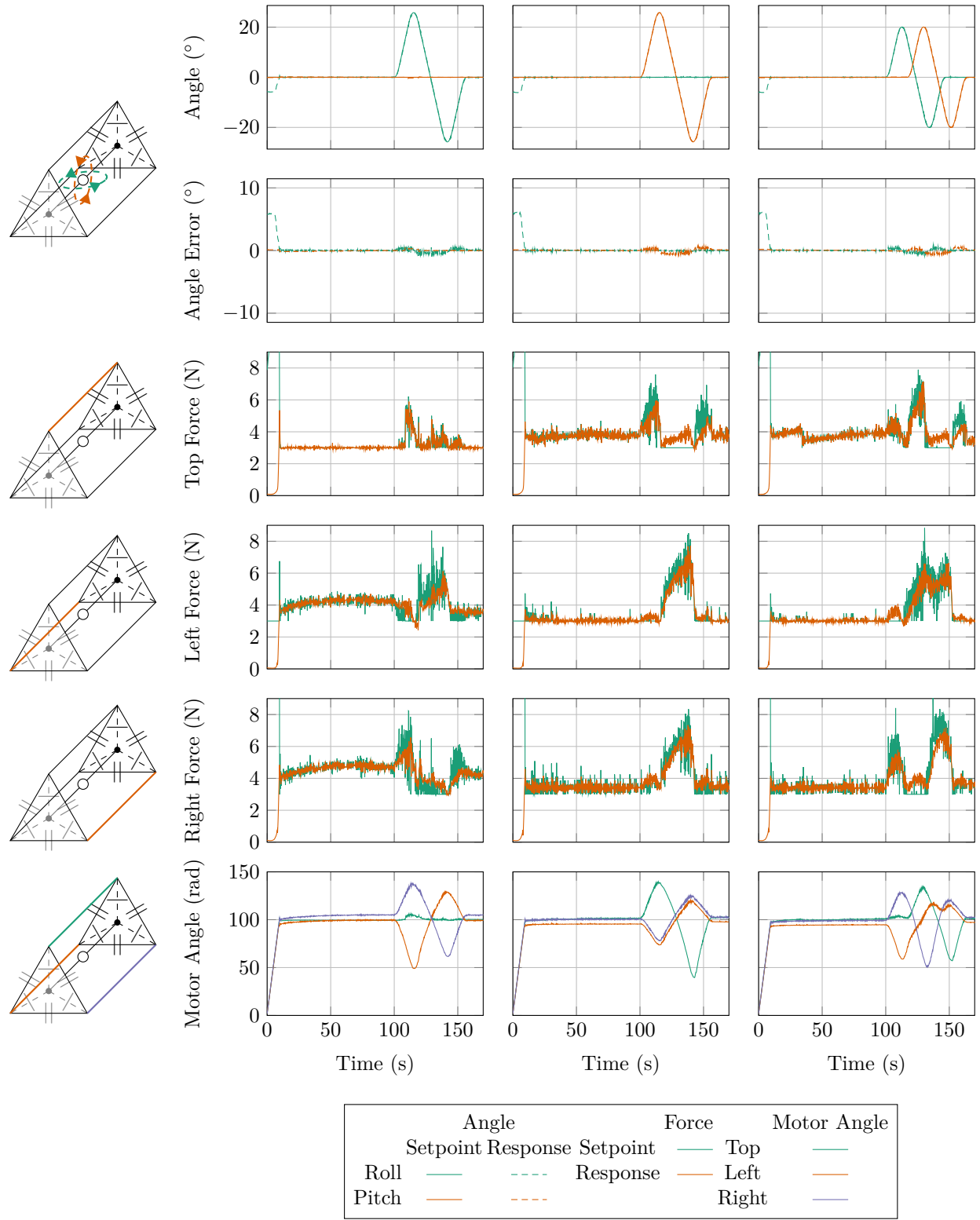


**Figure 10.** Plots of the response for three different trajectories, one on only the roll axis  $\theta_1$  (column 1), one on only the pitch axis  $\theta_2$  (column 2), and one on both axes  $\theta_1$  and  $\theta_2$  (column 3). Plots include AUJ orientation, forces at the top, left and right TSA, and the motor positions.

**3.2.2 AUJ Angle Measurement Accuracy** Figure 11 shows the difference between the BNO080 IMU and PDB08 potentiometer when the AUJ is at rest. The minimum measured change in value was  $0.21^\circ$  for the BNO080 and  $0.11^\circ$  for the PDB08, a significant increase in measured accuracy.

## 4 Additional Experimental Results

### 4.1 The Effect of Follower Mass on AUJ Angle Tracking

For a multi-segment design, analyzing the AUJ performance with a non-negligible follower mass is crucial. This addition alters the system dynamics,

**Table 4.** Summary of all the performance improvements and the measurements used to quantify them.

Improvement	Measurement	Results	
		Original	Improved
Increasing AUJ angle range	Maximum AUJ angle	14.50°	26.00°
Improving AUJ angle measurement accuracy	Minimum step change in AUJ angle measurement.	0.21°	0.10°
Preventing string failure	String failed when $f \leq 9?$	✓	✗

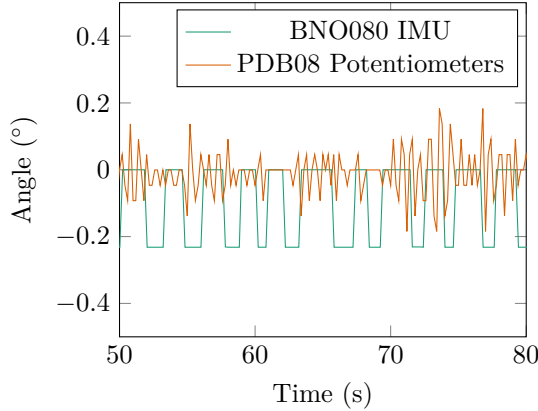


**Figure 11.** Comparison of the roll ( $\theta_1$ ) angle signal from the BNO080 IMU and PDB08 potentiometer when the AUJ is at rest at setpoint  $\theta = [0 \ 0]$ .

**Table 5.** Table of all the follower mass configurations, with the parameters for follower mass  $m$  and follower COM z offset  $\rho_3$ .

Config.	$m$ [g]	$\rho_3$ [mm]	$I$ [kg m <sup>-2</sup> ]	Image
No Mass	61.60	3.05	diag $\left( \begin{bmatrix} 2.80 \times 10^{-5} \\ 2.60 \times 10^{-5} \\ 5.00 \times 10^{-6} \end{bmatrix}^\top \right)$	
+20 g	81.29	15.74	diag $\left( \begin{bmatrix} 6.90 \times 10^{-5} \\ 6.80 \times 10^{-5} \\ 7.00 \times 10^{-6} \end{bmatrix}^\top \right)$	
+50 g	111.10	26.39	diag $\left( \begin{bmatrix} 1.06 \times 10^{-4} \\ 1.05 \times 10^{-4} \\ 1.10 \times 10^{-5} \end{bmatrix}^\top \right)$	
+80 g	140.35	32.44	diag $\left( \begin{bmatrix} 1.29 \times 10^{-4} \\ 1.27 \times 10^{-4} \\ 1.20 \times 10^{-5} \end{bmatrix}^\top \right)$	

affecting the inverse dynamic calculations in the control system, as illustrated in table 5. In figure 12, the response for a roll trajectory with varying follower body masses (20.00 g, 50.00 g, and 80.00 g) is depicted.

**Table 6.** Trapezoidal trajectory sequence parameters.

Cycle	Max./Min. Angle [rad]	Max. Velocity [rad s <sup>-1</sup> ]	Acceleration [rad s <sup>-2</sup> ]
1	0.40	0.40	$1.00 \times 10^{-2}$
2	0.40	0.44	$1.10 \times 10^{-2}$
3	0.40	0.48	$1.21 \times 10^{-2}$
4	0.40	0.53	$1.33 \times 10^{-2}$

Due to load cell safety limit of 9.00 N, larger masses could not be tested. Initially, setting  $k_p$  to the value in table 2 failed to achieve a steady state except for the “No Mass” configuration. By reducing  $k_p$  to 8000 in weighted configurations, a steady state was achieved with a maximum tracking error of 0.85°, similar to initial experiments. However, for the “No Mass” configuration, setting  $k_p$  to 8000 resulted in a poor tracking error of 3.06°, contrasting with the 0.76° maximum tracking error obtained with  $k_p$  from table 2. In future implementations, gain scheduling could optimize  $k_p$  selection for a given follower mass, minimizing tracking error while ensuring a steady state.

## 4.2 The Effect of AUJ Angular Velocity on AUJ Angle Tracking

To assess the AUJ performance at higher angular velocities, we repeated the experiments from section 3.2.1, but for each single axis. Using a trapezoidal “chirp” signal, we reduced the angle range to  $\pm 23.00$ ° to prevent overshoot. Each cycle increased the maximum angular velocity by  $\omega_0 + (2(n-1)\omega_0)$  and the angular acceleration by  $\alpha_0 + (16(n-1)\alpha_0)$ , where  $n$  is the cycle number and  $\omega_0$  and  $\alpha_0$  are initial values. Four cycles were executed, with the maximum velocity and acceleration values detailed in table 6. Figure 13 displays the experiment results, demonstrating a slight increase in tracking error with rising maximum angular velocity and acceleration. However, the pitch experiment could not be completed due to the load cell force exceeding the safety limit of 9.00 N, as evident in the figure.

## 5 Discussion

### 5.1 Active Transmission Adjustment (ATA)

The TSA mechanism exhibits a non-linear transmission ratio dependent on  $\theta_s$  (see Figure 14). This leads to an inverse relationship between the maximum stroke velocity  $\dot{p}_{\max}$  and maximum tensile force  $f_{\max}$  as  $\theta_s$  increases. Using the jacobian from (Nedelchev et al. 2020),  $f_{\max}$  and  $\dot{p}_{\max}$  are found as

$$\begin{aligned} \mathcal{J} &= \frac{\theta_s r_s^2}{l_u - p} \\ \mathcal{J}^{-1} &= \frac{l_u - p}{\theta_s r_s^2} \\ f_{\max} &= \mathcal{J}^{-1} \tau_{\max} \\ \dot{p}_{\max} &= \mathcal{J} \dot{\theta}_s \max. \end{aligned} \quad (4)$$

Thus, increasing  $\theta_s$  decreases  $f_{\max}$  and increases  $\dot{p}_{\max}$  for the same stroke  $p$ , with a greater effect if  $p$  increases.

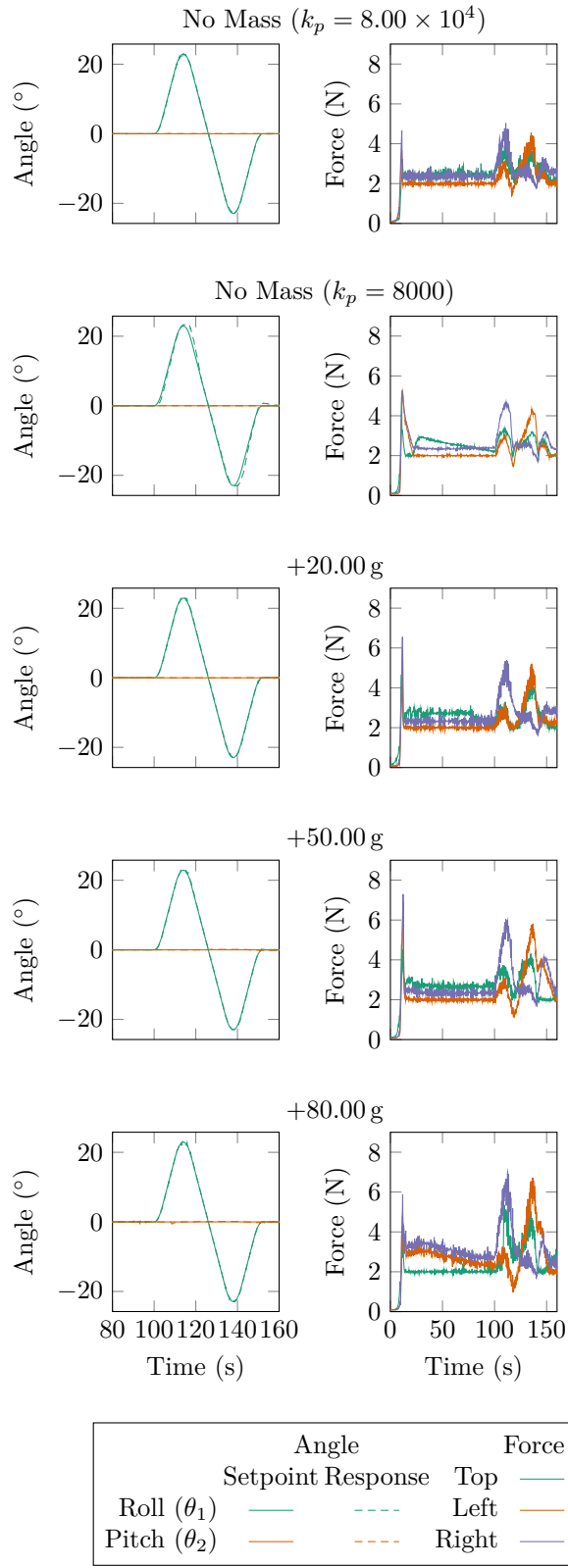


**Figure 12.** AUJ roll tracking with increasing follower mass from table 5, plus with no mass at  $k_p = 8000$  and  $k_p = 8.00 \times 10^4$ .

Adjusting  $f_{\min}$  requires increasing the minimum value of  $\theta_s$  for each TSA. This real-time alteration of  $f_{\min}$  can modify TSA and AUJ performance during operation, allowing for maximum joint torque to be increased at the expense of joint velocity, or vice versa.

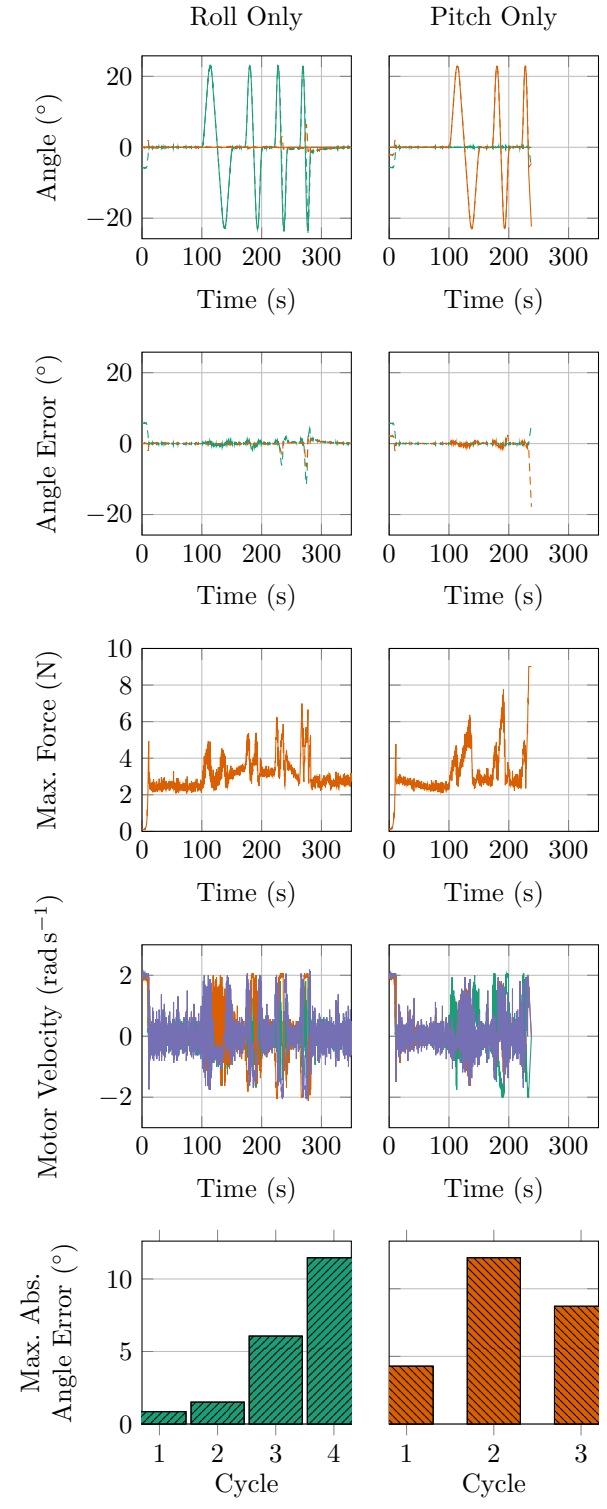


**Figure 13.** Results of the trapezoidal velocity trajectory from table 6 for both AUJ pitch and roll trajectories, including the maximum absolute angle error for each cycle.

It may be noticed that  $\lim_{\theta_s \rightarrow 0} f_{\max} = \infty$ , which is a consequence of assuming infinite material stiffness for the strings, which is not possible outside simulation.

This poses a challenge for real-world high force applications, as discussed in (Nedelchev et al. 2020).

With the simulation of the mechanism used in Crosby et al. (2022) using the AUJ trajectory from figure 10, a parameter sweep of  $f_{\min} = \{3.00, 4.00, 5.00, 6.00, 7.00, 8.00\}$  shows the expected increase in total motor torque  $\sum_{i=1}^3 \tau_i(t)$  and total TSA force  $\sum_{i=1}^3 f_i(t)$  for increasing values of  $f_{\min}$ , as shown in figure 15. Attempts were made to verify this experimentally with a modified parameter sweep to stay within load cell limits, however due to motor properties like gearbox backlash and PWM control nature, it was not possible to determine this relationship as the motor torque could not be measured accurately. Future work could explore better analysis methods or consider using brushless DC motors to enable experimental validation.

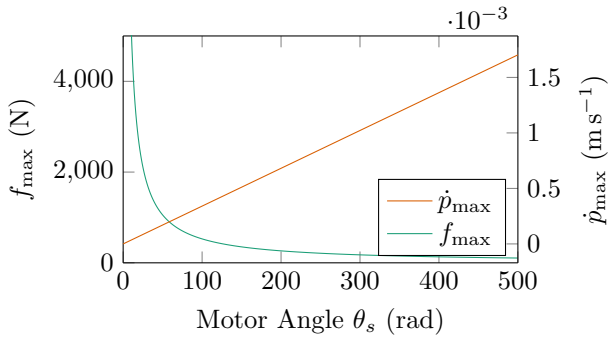


**Figure 14.** By adjusting  $f_{\min}$ , the transmission ratio of the TSA can be altered. Reducing  $f_{\min}$  increases the maximum TSA force  $f_{\max}$  while reducing the maximum TSA stroke velocity  $\dot{p}_{\max}$ . Conversely, increasing  $f_{\min}$  reduces  $f_{\max}$  and increases  $\dot{p}_{\max}$ . This can be used to actively modify the dynamic properties of the AUJ during operation. In this graph,  $p = 0$ .

## 5.2 Dynamics Gravity Vector

In the experiments,  $\mathbf{g}$  was assumed parallel to the  $z$  axis ( $[0 \ 0 \ -9.81]$ ) due to the vertical orientation of the mechanism. To function in other orientations, an IMU would be necessary to compute the gravity vector, incorporating gyroscopes to counter motion-generated forces.

## 5.3 Load Cell Limitation

As noted in sections 3.2.1, 4.1 and 4.2, the load on each TSA being limited to 9.00 N meant that the AUJ angle range was limited with an increased follower mass, increased velocity, and in dual axis operation. Using load cells with a larger full scale would increase the AUJ angle range in all cases.

## 5.4 Multi-Segment Design

One potential practical application of this mechanism is to chain multiple TSA AUJ together to create a flexible robot comprised of multiple segments. Snake and snake-arm robots are common implementations of chains of AUJ where this mechanism could be implemented.

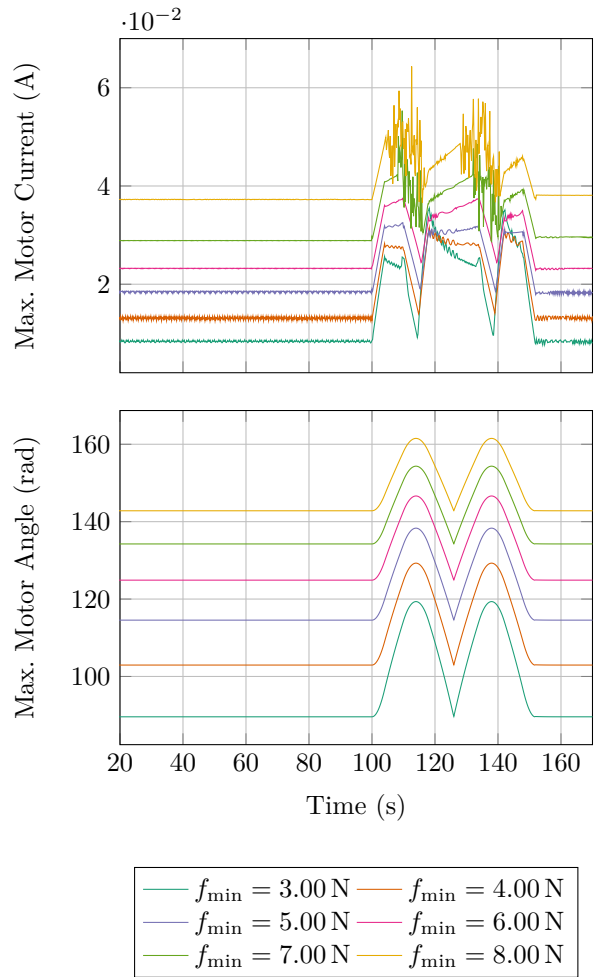


**Figure 15.** Sum of TSA maximum motor currents and angles for a simulated roll ( $\theta_1$ ) trajectory from figure 10 at different values of  $f_{\min}$ .

Snake robots in particular are a promising application, since the actuators need to be inline unless the snake robot is tethered, and segment mass is an important factor for agility, manoeuvrability and accommodation of batteries and sensor packages.

**5.4.1 Self-Supporting Segments Limit** If we consider a multi segment design of an arbitrary identical segments of mass  $m$ , length  $l$  and center of mass (COM) offset  $\rho$  along the  $z$  axis, this can be defined as the maximum number of segments in that can be supported with no contact points under the influence of gravity  $\mathbf{g}$  in any orientation. This is important for snake robots, as it determines how far they can reach when performing certain manoeuvres that require vertical traversal, such as climbing stairs. For snake-arm robots, it effectively is the limit for the number of segments, since all segments are continuously operating with no contact points. This limit  $n_{\lim} \in \mathbb{N}$  is defined by

$$\begin{aligned} \tau_{\max} &\geq \sum_{i=0}^{n-1} m(i\ell + \rho) \\ &\geq mg \left( n\rho + \frac{\ln(n-1)}{2} \right) \quad (5) \\ n_{\lim} &= \left\lfloor \frac{1}{2} - \frac{\rho - \sqrt{\frac{l^2}{4} - l\rho + \rho^2 + \frac{2l\tau_{\max}}{mg}}}{l} \right\rfloor \end{aligned}$$

which can be generalised to include designs with heterogeneous segments. Calculating  $\tau_{\max}$  depends on the design of the actuation system. For “direct drive” motor driven systems, it is simply the maximum rated torque of the motor. For cable or linear actuator driven systems, it is  $f_{\max}r$ , where  $f_{\max}$  is the maximum rated force of the actuator, and  $r$  is the radius distance from the actuator to the pivot axis. For TSA actuators, this is extended to  $\mathcal{J}^{-1}\tau_{\max}r$ , as shown in equation 4.

Table 7 gives a list of snake robots with inline actuators, identical segments, and their self-supporting segments limit. *Uncle Sam* and *SEA Snake* both have 16 segments of alternating 1 DOF joints, each pair of these is considered one segment in this analysis. Segment COM offsets are not provided, so it is assumed to be  $\frac{l}{2}$ .

We can then construct a theoretical snake robot made of the TSA AUJ segments in this publication, and see how it would compare to existing snake robots. However, since the prototype was constructed of lightweight 3D printed materials which are not designed to be durable, with a mass of only 61.60 g, a direct comparison would not be entirely fair. Therefore, we have considered designs with additional mass, weighing 300.00 g and 900.00 g respectively. Figure 16 shows the limit as  $\theta_s$  increases for a 20 segment robot, which outperforms all of the robots in table 7 within 200.00 rad, whereas the experiments conducted in section 4 have a maximum motor angle of 139.80 rad, as shown in figure 10. There are limitations to this analysis, as it only uses a simple model for the TSA that does not take into account string compliance and friction, therefore physical implementations are not expected to perform as well. Most of the snake robots in table 7 also have a larger joint angle range than the prototype design, which may be useful for some tasks, such as anchoring to a tree. However, it shows that the TSA AUJ mechanism has a lot of potential in developing highly mobile snake robots with a large number of segments that are able to self-support the majority of said segments, which would allow for increased agility in many environments. It also allows for similarly long snake-arm robots with inline actuation.

**5.4.2 Distributed Control System** In a multi-segment setup, individual embedded control systems within each segment could receive AUJ angle position setpoints from a central controller. This setup enables the execution of complex trajectories while minimizing wiring complexity through shared power and communication buses, fostering a modular design. Figure 17 shows a conceptual system diagram for this setup.

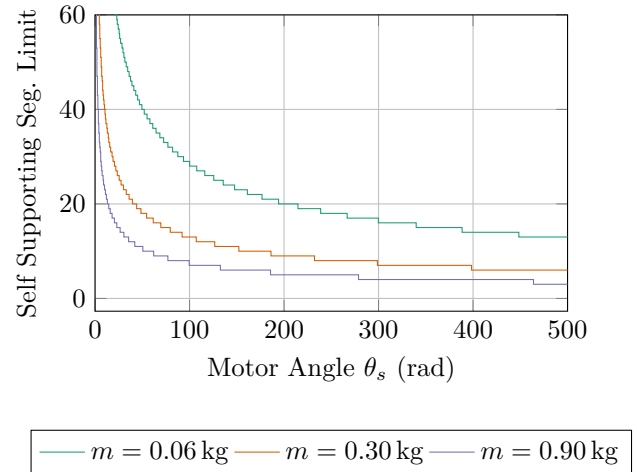


**Figure 16.** Graph showing the decrease in self-supporting segments limit as TSA motor angle  $\theta_s$  increases for different segment masses  $m$ . Segment length is 155.00 mm measured from the prototype, other coefficients as used in figure 14 from table 2.

## 6 Conclusion

This publication examines an existing prototype of an actuated universal joint with twisted string actuator to pinpoint enhancements and address limitations. Three key design improvements were identified and tested, resulting in an expanded AUJ angle range from  $\pm 14.50^\circ$  to  $\pm 26.00^\circ$ , increased AUJ measurement accuracy from  $0.21^\circ$  to  $0.11^\circ$ , and zero recorded string failures under normal conditions. Additionally, the impact of added follower mass on AUJ performance was assessed to simulate multi-segment operation. Future efforts will focus on resolving remaining limitations, including installing load cells with larger full scales, developing a distributed control system for multi-segment operation, and exploring effective methods for measuring motor current under pulse width modulation (PWM) control or using brushless DC motors for accurate ATA assessment.

## Funding

The author(s) disclosed receipt of the following financial support for the research, authorship, and/or publication of this article: This work was supported by a UKRI EPSRC Doctoral Training Partnership [1957210], and by the UKRI Strength in Place Fund [84646 (AMPI)].

## Declaration of conflicting interests

The author(s) declared no potential conflicts of interest with respect to the research, authorship, and/or publication of this article.

## Supplemental material

A video demonstrating the results from section 3.2.1 is available as supplementary material online.

## Acknowledgements

The lead author wishes to thank Dr. Dmitriy Makhnovskiy for his assistance in preliminary research for this publication.

**Table 7.** List of snake robots, their number of segments  $n$ , their segment mass  $m$ , segment length  $l$ , maximum joint torque  $\tau_{\max}$ , and self-supporting segment limit.

Robot Name	Image	$n$	$m$ [kg]	$l$ [mm]	$\tau_{\max}$ [N m]	Limit
Uncle Sam (Wright et al. 2012)		8	0.32	101.60	1.30	2
SEA Snake (Rollinson et al. 2014)		8	0.41	128.00	7.00	5
Zmeelok-3M (Varlashin and Shmakov 2019)		10	0.40	80.00	3.20	4
ACM-R5 (Yamada 2005)		9	0.80	170.00	9.00	3
Wheeko (Liljebäck et al. 2013)		10	0.96	130.00	4.50	2

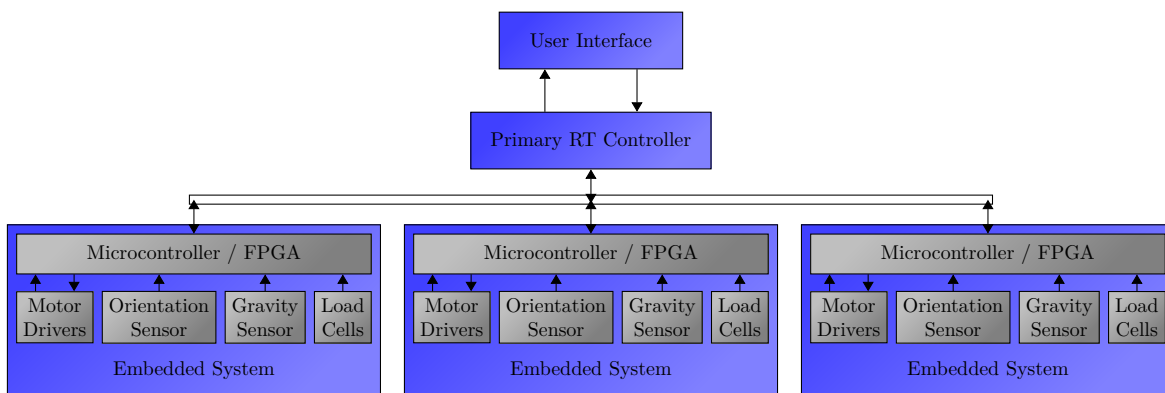


**Figure 17.** Proposed system architecture for a future multi-segment system. Each segment has an embedded controller programmed with the cascaded control loop. The controller interfaces with the load cells for each TSA, the orientation sensors for the AUJ, an accelerometer to provide the local gravity vector for dynamics calculations, and the drivers for the TSA motors. A primary controller then uses a common control bus to interface with the embedded controllers, reading and writing data to registers to issue motion commands and get status updates.

## 7 Author Contributions

### References

- Baba T, Kameyama Y, Kamegawa T and Gofuku A (2010) A snake robot propelling inside of a pipe with helical rolling motion. In: *Proceedings of SICE Annual Conference 2010*. IEEE, pp. 2319–2325.
- Bienczyk K (2009) Angle measurement using a miniature hall effect position sensor. In: *2009 2nd International Students Conference on Electrodynamic and Mechatronics*. IEEE, pp. 21–22.
- BNO080 Data Sheet (2017) *BNO080 Data Sheet*. Hillcrest Laboratories, Inc., 1.3 edition.
- Budynas R and Nisbett J (2011) *Shigley's Mechanical Engineering Design*. McGraw-Hill series in mechanical engineering. McGraw-Hill. ISBN 9780071328401.
- Crosby D, Carrasco J, Heath W and Weightman A (2022) A novel triad twisted string actuator for controlling a two degrees of freedom joint: Design and experimental validation. In: *2022 International Conference on Robotics and Automation (ICRA)*. IEEE, pp. 11388–11394.
- DC Micromotors - Precious Metal Commutation (2020) *DC Micromotors - Precious Metal Commutation*. Dr. Fritz Fauhaber GmbH & Co. KG.
- Dessen F (1986) Coordinating control of a two degrees of freedom universal joint structure driven by three servos. In: *Proceedings. 1986 IEEE International Conference on Robotics and Automation*, volume 3. pp. 817–822. DOI:10.1109/ROBOT.1986.1087559.
- JL-12FN20-50-06420 (2020) *JL-12FN20-50-06420*. Guang-dong Kingly Gear Co.
- Konda R, Bombara D, Chow E and Zhang J (2023) Kinematic modeling and open-loop control of a twisted string actuator-driven soft robotic manipulator. *Journal of Mechanisms and Robotics* : 1–18.

- LCM100 Miniature In Line Load Cell (2024) *LCM100 Miniature In Line Load Cell*. FUTEK Advanced Sensor Technology Inc.
- Lee D, Kim DH, Che CH, In JB and Shin D (2019) Highly durable bidirectional joint with twisted string actuators and variable radius pulley. *IEEE/ASME Transactions on Mechatronics* 25(1): 360–370.
- Liljebäck P, Pettersen KY, Stavdahl Ø and Gravdahl JT (2013) *Snake robots: modelling, mechatronics, and control*. Springer.
- Motion Controllers - Series MCDC 3002 S (2018) *Motion Controllers - Series MCDC 3002 S*. Dr. Fritz Fauhaber GmbH & Co. KG, 6 edition.
- Muehlbauer P, Schimbera M, Stewart K and Pott PP (2021) Twisted string actuation for an active modular hand orthosis. In: *ACTUATOR; International Conference and Exhibition on New Actuator Systems and Applications 2021*. VDE, pp. 1–4.
- Nedelchev S, Gaponov I and Ryu J (2020) Accurate dynamic modeling of twisted string actuators accounting for string compliance and friction. *IEEE Robotics and Automation Letters* 5(2): 3438–3443. DOI:10.1109/LRA.2020.2970651.
- Palli G, Natale C, May C, Melchiorri C and Wurtz T (2012) Modeling and control of the twisted string actuation system. *IEEE/ASME Transactions on Mechatronics* 18(2): 664–673.
- Park J, Kim JH, Kim KS and Kim S (2016) Design and control of antagonistic robot joint with twisted string actuators. In: *2016 13th International Conference on Ubiquitous Robots and Ambient Intelligence (URAI)*. IEEE, pp. 563–565.
- Park J, Park Ji, Seo HT, Liu Y, Kim KS and Kim S (2020) Control of tendon-driven (twisted-string actuator) robotic joint with adaptive variable-radius pulley. In: *2020 20th International Conference on Control, Automation and Systems (ICCAS)*. IEEE, pp. 1096–1098.
- PDB08 - 8 mm Micro Rotary Potentiometer (2021) *PDB08 - 8 mm Micro Rotary Potentiometer*. Bourns.
- Popov D, Gaponov I and Ryu JH (2013) Bidirectional elbow exoskeleton based on twisted-string actuators. In: *2013 IEEE/RSJ International Conference on Intelligent Robots and Systems*. IEEE, pp. 5853–5858.
- Qin G, Cheng Y, Ji A, Pan H, Yang Y, Yao Z and Song Y (2023) Research on the cable-driven endoscopic manipulator for fusion reactors. *Nuclear Engineering and Technology*.
- Rezaei A, Shekofteh Y, Kamrani M, Fallah A and Barazandeh F (2008) Design and control of a snake robot according to snake anatomy. In: *2008 International Conference on Computer and Communication Engineering*. IEEE, pp. 191–194.
- Rollinson D, Bilgen Y, Brown B, Enner F, Ford S, Layton C, Rembisz J, Schwerin M, Willig A, Velagapudi P et al. (2014) Design and architecture of a series elastic snake robot. In: *2014 IEEE/RSJ International Conference on Intelligent Robots and Systems*. IEEE, pp. 4630–4636.
- Spong MW, Hutchinson S and Vidyasagar M (2020) *Robot modeling and control*. John Wiley & Sons.
- Suthar B and Jung S (2021) Design and feasibility analysis of a foldable robot arm for drones using a twisted string actuator: Frad-tsa. *IEEE Robotics and Automation Letters* 6(3): 5769–5775. DOI:10.1109/LRA.2021.3084890.
- Usman M, Suthar B, Seong H, Hawkes E, Gaponov I and Ryu JH (2017) Passive returning mechanism for twisted string actuators. In: *2017 IEEE International Conference on Robotics and Automation (ICRA)*. IEEE, pp. 3714–3719.
- Varlashin V and Shmakov O (2019) Comparative analysis of the virtual and physical experiments with a snake robot's rectilinear movement. In: *Journal of Physics: Conference Series*, volume 1326. IOP Publishing, p. 012037.
- Wright C, Buchan A, Brown B, Geist J, Schwerin M, Rollinson D, Tesch M and Choset H (2012) Design and architecture of the unified modular snake robot. In: *2012 IEEE international conference on robotics and automation*. IEEE, pp. 4347–4354.
- Würtz T, May C, Holz B, Natale C, Palli G and Melchiorri C (2010) The twisted string actuation system: Modeling and control. In: *2010 IEEE/ASME International Conference on Advanced Intelligent Mechatronics*. pp. 1215–1220. DOI:10.1109/AIM.2010.5695720.
- Yamada H (2005) S. development of amphibious snake-like robot acm-r5. In: *The 36th international symposium on robotics (ISR 2005), Tokyo*.